catalysts

MDPI

Article

Integrated p-n Junctions for Efficient Solar Water Splitting upon TiO_2/CdS/$BiSbS_3$ Ternary Hybrids for Improved Hydrogen Evolution and Mechanistic Insights

Bhagatram Meena [1], Mohit Kumar [1], Arun Kumar [1], Gudipati Neeraja Sinha [1], Rameshbabu Nagumothu [2], Palyam Subramanyam [3], Duvvuri Suryakala [4] and Challapalli Subrahmanyam [1,*]

[1] Department of Chemistry, Indian Institute of Technology Hyderabad, Hyderabad 502285, Telangana, India
[2] Department of Metallurgical and Materials Engineering, National Institute of Technology, Tiruchirappalli 620015, Tamil Nadu, India
[3] Research Institute for Electronic Science, Hokkaido University, Sapporo 001-0020, Hokkaido, Japan
[4] Department of Chemistry, GITAM University, Visakhapatnam 530045, Andhra Pradesh, India
* Correspondence: csubbu@iith.ac.in

Abstract: The development of efficient and novel p-n heterojunctions for photoelectrochemical (PEC) water splitting is still a challenging problem. We have demonstrated the complementary nature of (p-type) $BiSbS_3$ as a sensitizer when coupled with (n-type) TiO_2/CdS to improve the photocatalytic activity and solar to hydrogen conversion efficiency. The as-prepared p-n heterojunction TiO_2/CdS/$BiSbS_3$ exhibits good visible light harvesting capacity and high charge separation over the binary heterojunction, which are confirmed by photoluminescence (PL) and electrical impedance spectroscopy (EIS). The ternary heterojunction produces higher H_2 than the binary systems TiO_2/CdS and TiO_2/$BiSbS_3$. This ternary heterojunction system displayed the highest photocurrent density of 5 mA·cm^{-2} at 1.23 V vs. reversible hydrogen electrode (RHE) in neutral conditions, and STH of 3.8% at 0.52 V vs. RHE is observed. The improved photocatalytic response was due to the favorable energy band positions of CdS and $BiSbS_3$. This study highlights the p-n junction made up of TiO_2/CdS/$BiSbS_3$, which promises efficient charge formation, separation, and suppression of charge recombination for improved PEC water splitting efficiency. Further, no appreciable loss of activity was observed for the photoanode over 2500 s. Band alignment and interfaces mechanisms have been studied as well.

Keywords: solar water splitting; photoanode; ternary hybrid; $BiSbS_3$; nanospheres; p-n junction

Citation: Meena, B.; Kumar, M.; Kumar, A.; Sinha, G.N.; Nagumothu, R.; Subramanyam, P.; Suryakala, D.; Subrahmanyam, C. Integrated p-n Junctions for Efficient Solar Water Splitting upon TiO_2/CdS/$BiSbS_3$ Ternary Hybrids for Improved Hydrogen Evolution and Mechanistic Insights. *Catalysts* **2022**, *12*, 1117. https://doi.org/10.3390/catal12101117

Academic Editors: Yongpeng Liu and Yong Zuo

Received: 30 August 2022
Accepted: 22 September 2022
Published: 27 September 2022

1. Introduction

The negative impact of fossil fuels has driven the use of renewable fuels [1,2]. Hydrogen is considered as a promising energy source among all the potential candidates, owing to its gravimetric energy density and clean combustion [3–5]. PEC water splitting is a sustainable way for conversion of solar energy into chemical energy [6,7]. Various semiconductor metal oxides based on photoanodes such as TiO_2, WO_3, $BiVO_4$, ZnO, SnO_2, CeO_2, and Fe_2O_3 have been studied [8–14]. Among them, TiO_2 has been recognized as a potential candidate due to its non-toxicity, availability, cost efficiency, and high thermal and chemical stability. Despite these facts, its visible light activity is insignificant because of its limited solar light absorption in UV-region and high recombination rate of photoinduced charge carriers. TiO_2 has a bandgap of 3.2 eV. The very first report on TiO_2 photocatalysts was done by Fujishima and Honda in 1972 [15]. To overcome these challenges, various strategies have been introduced in recent studies such as cocatalyst loading, morphology modification, metal ion doping, surface plasmon resonance, and heterojunction formation. Among all these, heterojunction formation has gained much attention due to its nature of

suppressing the charge carrier recombination, improving the charge separation, and boosting the photocatalytic performance [16–19]. Heterojunction formation strategy has gained attention because they can effectively reduce the rate of electron–hole recombination [20].

Recently, various studies have been reported on heterojunction formation with narrow bandgap materials or metal chalcogenides materials such as Bi_2S_3, CdS, In_2S_3, Bi_2Se_3, and CdSe [8,9,16,21,22]. Among them, CdS has been studied widely even after such drawbacks such as instability in aqueous solution and toxicity, and its bandgap of 2.4 eV can broaden the absorption range of the solar spectrum. Another advantage of CdS is that the conduction band position of CdS is more negative than CB of TiO_2, so feasible electrons transfer can occur in CB, whereas holes transfer towards the opposite direction. This boosts the hydrogen evolution and oxygen evolution reactions. Various studies have been reported based on nanostructured photoelectrodes for solar water splitting using CdS exhibiting high current densities and solar to hydrogen efficiencies. Even then, a still narrow bandgap semiconductor is required to improve the photocatalytic performance and stability in aqueous solution of fabricated electrodes because it exhibits photocorrosion in an aqueous medium [23].

Although several ternary systems have been reported, such as TiO_2/CdS/CdSe and TiO_2/Ag_2Se/CdS, their performances have not been remarkable due to photocorrosion issues, (Table 1) but have shown better photoactivity than binary and single semiconductor-based photoelectrodes. In order to enhance the performance of the photoelectrode, $BiSbS_3$ has been introduced as a narrow bandgap semiconductor. $BiSbS_3$ is a p-type semiconductor with a bandgap of 1.85 eV and its conduction band and valence band position are feasible to hydrogen evolution reaction [24]. The constructed ternary system is expected to enhance PEC performance due to proper band edge positions, better charge transfers, and proper charge separation achieved by the type II band structure. The development of a p–n junction photoelectrode is recognized as a significant method for increasing electron–hole lifespan, improving charge carriers separation, and reducing charge carrier recombination. The transportation of holes and electrons in opposite directions causes an internal electric field at the p-n junction. Under solar light irradiation with an external bias, the generated internal electrical field at a p-n heterojunction can considerably improve effective charge separation and transportation, resulting in high quantum efficiency. As a result, by coupling anodic material photoelectrodes with a cathodic material to construct a nanostructured p-n heterojunction electrode, the PEC water-splitting solar to hydrogen efficiency of anodic material can be boosted. Mostly, such a coating will decrease photocorrosion as well as control surface energetics and kinetics [25]. In previous studies, $BiSbS_3$ had a suitable band edge position with TiO_2 to form a type II band structure at the edge of semiconductors with CdS band positions existing in between, which leads to efficient charge transportation and charge separation [26]. However, there is no report on the study based on a TiO_2/CdS/$BiSbS_3$ heterojunction photoanode.

Table 1. Comparison of fabricated photoanode TiO_2/CdS/$BiSbS_3$ with previous studies.

Sr. No.	Electrode Materials	Current Density	Electrolyte	References (Publishing Year)
1	TiO_2/CdS/Bi_2S_3	2.16 mA·cm^{-2}	0.25 M $Na_2S{\cdot}9H_2O$ + 0.35 M Na_2SO_3	[27], 2013
2	TiO_2/CdS/Co–Pi	0.35 mA·cm^{-2}	0.1 M sodium phosphate	[28], 2015
3	TiO_2/CdS/Cu_2ZnSnS_4	1.09 mA·cm^{-2}	0.25 M Na_2S + 0.35 M Na_2SO_3	[29], 2019
4	TiO_2@$BaTiO_3$/CdS	0.97 μA.cm^{-2}	0.2 M Na_2SO_4	[30], 2022
5	Ti_3CN@TiO_2/CdS	1.2 μA.cm^{-2}	0.2 M Na_2SO_4	[31], 2021
6	1D TiO_2/CdS/ZnS	5.84 mA·cm^{-2}	0.3 M Na_2SO_3 + 0.25 M Na_2S	[32], 2021
7	TiO_2/CdS/CdSe	0.44 mA·cm^{-2} at 1.23 V vs. cathode	0.5 M Na_2SO_4	[33], 2021

Table 1. *Cont.*

Sr. No.	Electrode Materials	Current Density	Electrolyte	References (Publishing Year)
8	$TiO_2/Sb_2S_3/rGO$	0.039 mA·cm^{-2}	0.1 M Na_2SO_4	[34], 2021
9	$TiO_2/In_2S_3/CdS$	0.18 mA·cm^{-2}	0.25 M Na_2S + 0.35 M Na_2SO_3	[35], 2019
10	$TiO_2/CdS/BiSbS_3$	5.0 mA·cm^{-2}	0.1 M Na_2SO_4	In this Work

In this study, we developed a p-n heterojunction $TiO_2/CdS/BiSbS_3$ ternary hybrid for efficient solar water splitting. TiO_2 was coated by the doctor blade method and annealing process at 500 °C for 30 min. Followed by deposition of CdS to fabricate an efficient photoanode, five SILAR (successive ionic layer adsorption and reactions) cycles were completed using cadmium acetate as the Cd precursor and sodium sulphide as the S precursor. Then, using the chemical bath deposition (CBD) method, $BiSbS_3$ was coated over TiO_2/CdS, and this was followed by an annealing process under argon flow at 300 °C for 1 h. Bismuth chloride, antimony chloride, and acetamide were used as the precursors for the Bi^{+3}, Sb^{+3}, and S^{-2} ions, respectively. The fabricated ternary heterojunction exhibits enhanced PEC performance compared to binary heterojunction and bare semiconductor photoelectrodes. The highest current density displayed by ternary heterojunction is 5 mA·cm^{-2}, at 1.23 V vs. RHE, which is higher than binary heterojunctions in neutral electrolyte. The UV-visible spectra reveals that the ternary system exhibits more enhanced light harvesting capability than binary heterojunction. In addition, EIS and PL also reveal that charge separation and transportation is feasible compared to binary heterojunction. Thus, the enhanced PEC performance of the fabricated ternary heterojunction is attributed to the improved absorption capability and feasible charge transfer and separation. Hydrogen evolution also reveals that ternary heterojunction exhibits better photoactivity than binary heterojunction.

2. Results and Discussion

Optical Studies

To investigate the phenomenon of absorption with respect to fabricated electrodes from the solar spectrum, UV-Vis spectroscopy was taken into consideration as shown in Figure 1, where *x* and *y*-axis correspond to wavelength and (A) absorbance and a.u. is arbitrary unit, respectively. The UV-visible spectra of bare TiO_2 and CdS have been provided in the supporting information in Figure S1a,b. Bare TiO_2 exhibits a very low current density because of its band edge at 384 nm in the UV region, whereas bare CdS displays the band edge at 481 nm and bare $BiSbS_3$ exhibits a broad absorption spectrum at 670 nm. Compared to bare electrodes, composite electrodes absorb more visible light and display a red shift in wavelength. $TiO_2/CdS/BiSbS_3$ exhibits a greater red shift in wavelength than binary TiO_2/CdS and $TiO_2/BiSbS_3$ in the visible light region. Additionally, with the help of Tauc's equation, the optical bandgap of the samples were measured (bandgap calculation shown in supporting information). As shown in Figure 1d, the bandgap energies of the films made of $TiO_2/BiSbS_3$, TiO_2/CdS, and $TiO_2/CdS/BiSbS_3$ are, respectively, 1.52, 2.40, and 1.81 eV. As calculated by a Tauc's plot, as shown in Figure S2, TiO_2, $BiSbS_3$, and CdS have direct bandgaps of 3.2, 1.85, and 2.58 eV, respectively. Furthermore, the following equation can be used to measure the light harvesting efficiency (LHE) of the photoactive materials: LHE = $1–10^{-A}$, where A is the absorbance at wavelength [36] and the results that have been presented in Figure 1c $TiO_2/CdS/BiSbS_3$ notably exhibit a higher LHE than the TiO_2/CdS, which is matched with the absorption spectrum measurements. Based on these observations, increasing light absorption makes it possible to absorb more photons and therefore produce more excitons, which promotes higher current densities for PEC water splitting.

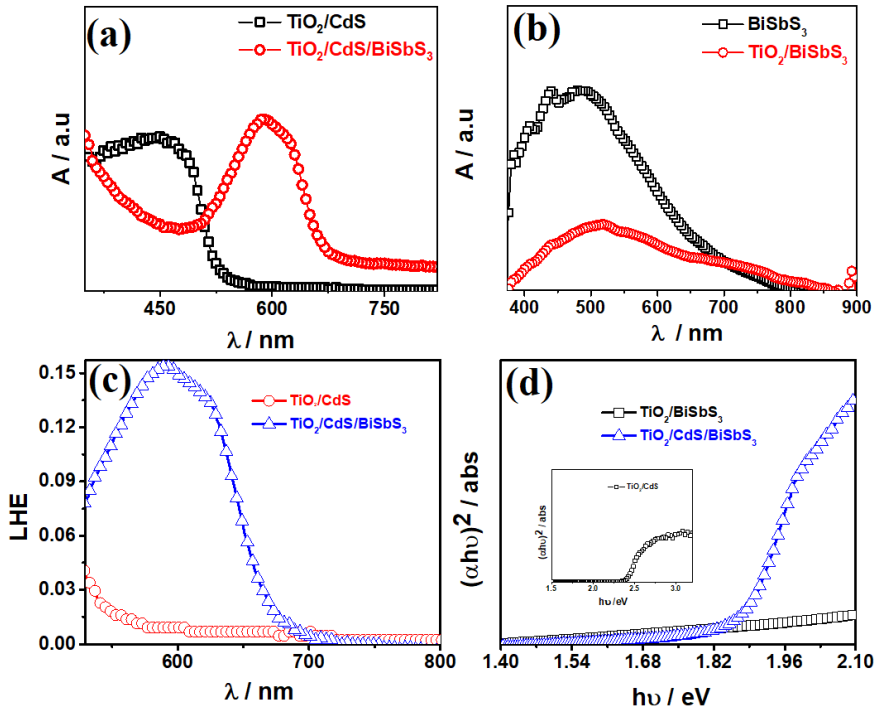

Figure 1. Fabricated electrodes (**a**,**b**), UV-Visible spectra (**c**) LHE efficiency, and (**d**) Tauc's plots.

The lifetime of the photoinduced electron–hole pairs in the heterojunctions under irradiation can be investigated by photoluminescence (PL) spectra as shown in Figure S3. The greater the lifetime of the photogenerated electrons, the weaker the photoluminescence emission, implying that composites have better PEC activity. The visible region shift is responsible for the high PL emission peaks seen in $TiO_2/BiSbS_3$ and TiO_2/CdS, compared to $TiO_2/CdS/BiSbS_3$, which are about 580 nm. As seen by its attenuated PL peaks, $TiO_2/CdS/BiSbS_3$ has the weakest electron–hole recombination rate.

XRD patterns of the constructed photoelectrodes namely, TiO_2, $BiSbS_3$, $TiO_2/BiSbS_3$, and $TiO_2/CdS/BiSbS_3$ are shown in Figure 2 and it confirms their formation. XRD patterns of bare TiO_2 and $BiSbS_3$ are given in Figure 2 and are well-matched with JCPDS #89-4921 and ICDS-617029, respectively. A bare CdS XRD pattern is given in Figure S4, which is well- matched with JCPDS #65-2887. The XRD pattern of TiO_2 indicates the peaks with d-spacing of 3.51, 2.43, 2.36, 1.89, 1.69, 1.66, 1.47, 1.36, and 1.33 Å, corresponding to TiO_2 planes (101), (103), (004), (200), (105), (211), (204), (116), and (220), respectively. TiO_2 anatase exhibits a body-centered tetragonal structure that resembles JCPDS #89-4921. Similarly, $BiSbS_3$ planes correspond to given crystallographic database ICDS -617029, which confirms their purity. Similarly, the face-centered cubic structure of CdS was also confirmed using (111), (220), and (311) planes, which correspond to 3.32, 2.06, and 1.75 Å d-spacing values, respectively (JCPDS-652887). In the case of $TiO_2/BiSbS_3$ and TiO_2/CdS XRD, patterns match with JCDPS data. Ternary heterojunction $TiO_2/CdS/BiSbS_3$ display all the peaks, which confirms the successful formation of electrodes. In both $TiO_2/BiSbS_3$ and $TiO_2/CdS/BiSbS_3$ heterojunction nanocomposites, $BiSbS_3$ can maintain its own crystal form. Peak intensities of $TiO_2/BiSbS_3$ and $TiO_2/CdS/BiSbS_3$ increase at around 25.25°, which can be understood by the peak superposition of TiO_2 at 25.34, $BiSbS_3$ at 24.94°, and the CdS peak at 26.62°. The XRD patterns of $TiO_2/BiSbS_3$ and $TiO_2/CdS/BiSbS_3$ composites reveal well formation of TiO_2, $BiSbS_3$, and CdS phases [37,38].

To further conclude the successful formation of the ternary p-n heterojunction $TiO_2/CdS/BiSbS_3$, X-ray photoelectron spectroscopy measurements were taken into the account. The XPS analysis was recorded to find the existence of indivisible elements such as Ti, O, Cd, S, Bi, and Sb elements in the ternary heterojunction. As shown in Figure S5, the binding energy (BE) levels were calibrated to the C 1s peak at 284.6 eV. Figure 3a shows the multiple

peaks in $TiO_2/CdS/BiSbS_3$ with a spin-orbital difference of 5.74 eV at binding energies of 458.36 eV and 464.1 eV, respectively. These peaks seem regular and comparable with Ti^{4+} in TiO_2, and they correspond to prior findings [39]. At 529.6 eV, the O 1s spectrum of TiO_2 matches lattice oxygen, as seen in Figure 3b (Ti-O-Ti). The $3d_{3/2}$ and $3d_{5/2}$ binding energies of Cd^{2+} species, are characterized by significant peaks at 412.0 and 405.3 eV in the Cd-3d XPS spectra Figure 3c, respectively [40]. The Bi-4f binding energy values revealed the existence of Bi^{3+} in the XPS spectra in Figure 3d, which may be deconvoluted into two peaks at 164.4 eV for Bi-$4f_{5/2}$ and 159.1 eV for Bi-$4f_{7/2}$. In Figure 3e, S-2p has two deconvoluted peaks of S 2p3/2 and S 2p1/2 at 160.3 and 162.2 eV, respectively [41]. Sb exhibited deconvoluted Sb $3d_{5/2}$ and Sb $3d_{3/2}$ peaks at 530.3 and 541.7 eV BE, respectively, in Figure 3f [42]. This evidence supports the development of a ternary heterojunction.

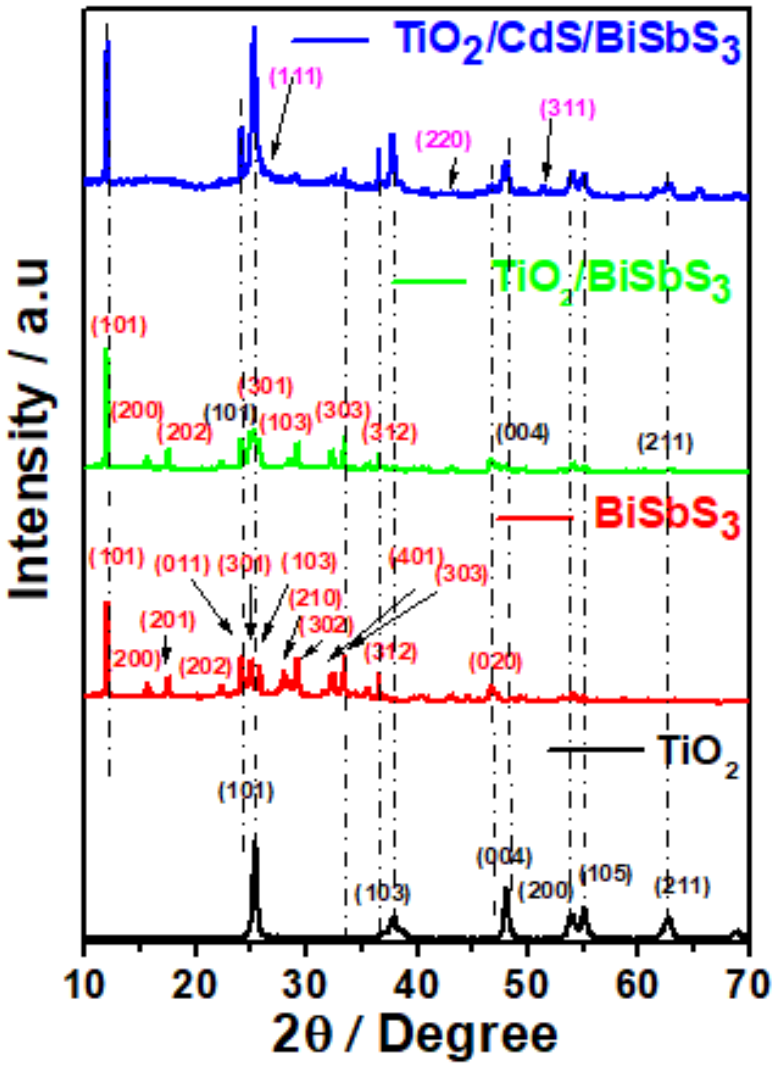

Figure 2. XRD patterns of fabricated electrodes (Black color is related to TiO_2, Red color corresponds to $BiSbS_3$, whereas Magenta color is related to CdS).

The morphology and microstructural formation of the bare p-type $BiSbS_3$ and p-n heterojunction $TiO_2/CdS/BiSbS_3$ ternary hybrid were analyzed by using FESEM. Bare TiO_2 SEM image and EDS (in Figure S12). It has a morphology of nanoparticles with a length and width of 25–40 nm. $BiSbS_3$ exhibits nanospherical morphology with a diameter of around 1.2 µm as shown in Figure 4a. In the case of binary heterojunction (as shown in Figure 4c), CdS was deposited over TiO_2 by the SILAR method that has dendrite-like morphology. Core material TiO_2 has nanoparticle morphology as shown in Figure 4b.

$BiSbS_3$ nanospheres can be seen above CdS (in Figure 4b). Elemental mappings have been given in Figure S6. Further EDS was performed to examine the existence of elements wherein the following elements Ti, O, Cd, Bi, Sb, and S were detected in the ternary heterojunction $TiO_2/CdS/BiSbS_3$ as shown in Figure 4d.

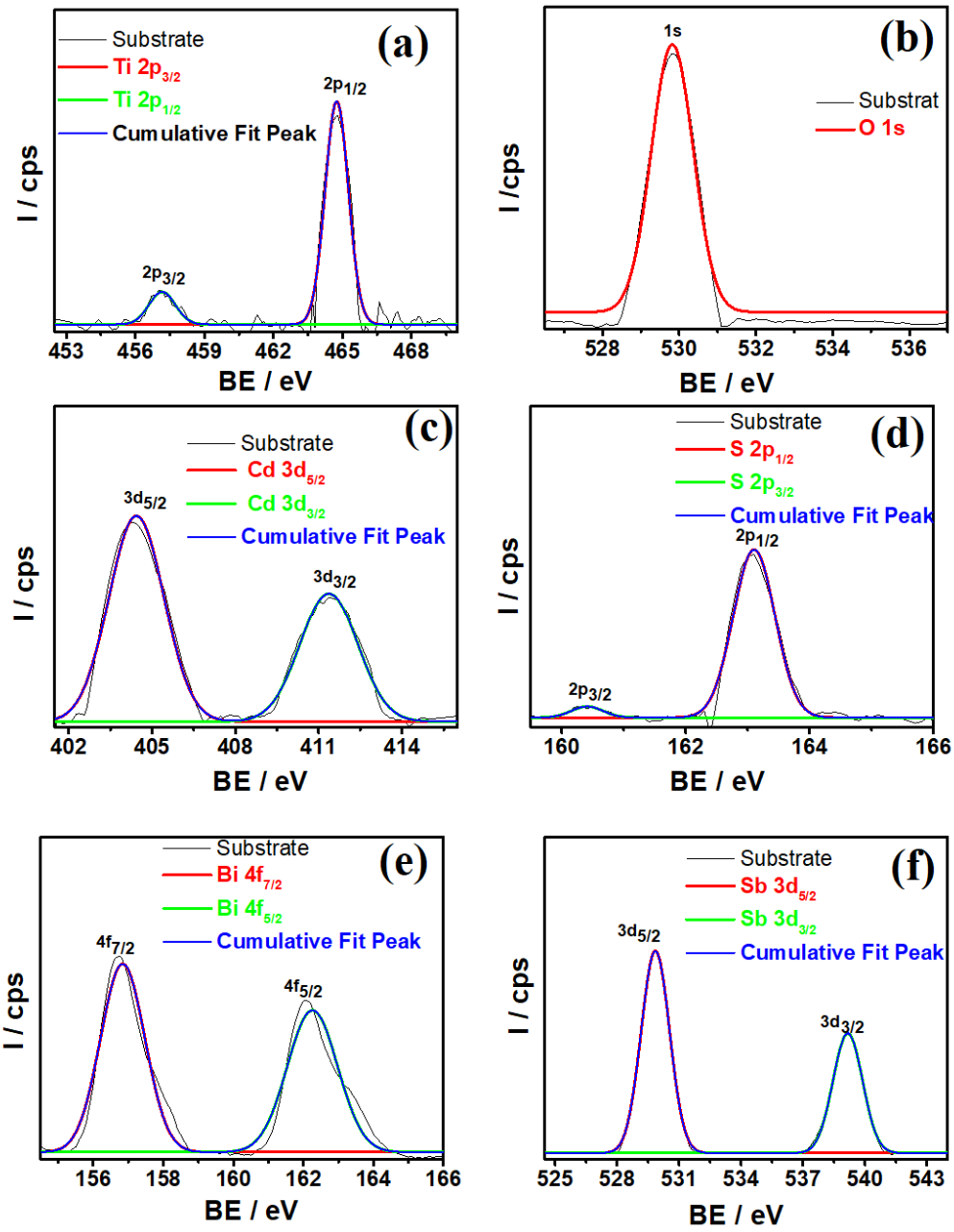

Figure 3. XPS spectra of (**a**) Ti 2p, (**b**) O 1s, (**c**) Cd 3d, (**d**) S 2p, (**e**) Bi 4f, and (**f**) Sb 3d.

To further confirm the morphology of prepared heterojunctions of TiO_2/CdS and $TiO_2/CdS/BiSbS_3$, HRTEM was recorded. HRTEM images of TiO_2/CdS displayed that the CdS layer is formed over TiO_2 nanoparticles as shown in Figure S7a. In the TiO_2/CdS heterojunction photoanode, all the lattice fringes are well-matched with XRD data as shown in Figure S7b. The HRTEM image of the $TiO_2/CdS/BiSbS_3$ photoanode reveals that TiO_2 NPs, CdS, and $BiSbS_3$ nanospheres are present in the composite as shown in Figure 4e,f. The lattice fringes of the $TiO_2/CdS/BiSbS_3$ photoanode in the composite are in good agreement with the XRD data.

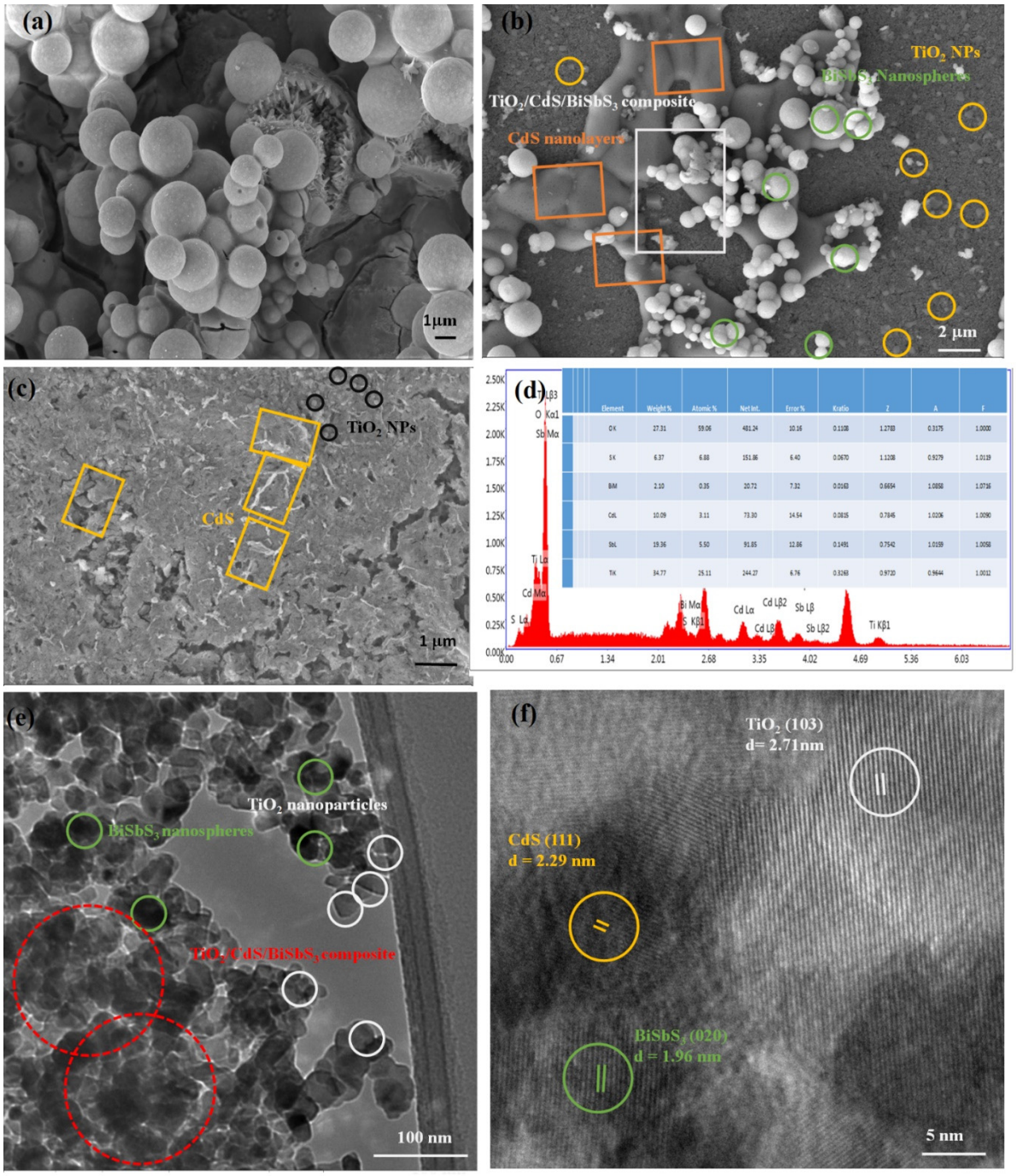

Figure 4. SEM images of (**a**) $BiSbS_3$, (**b**) $TiO_2/CdS/BiSbS_3$, (**c**) TiO_2/CdS (boxes are correspond to CdS and circles are for TiO_2 nanoparticles), (**d**) EDAX image of $TiO_2/CdS/BiSbS_3$, (**e**) HRTEM image of $TiO_2/CdS/BiSbS_3$ photoanode, and (**f**) lattice fringes of fabricated $TiO_2/CdS/BiSbS_3$ photoanode.

Further, the photocatalytic activity was recorded for fabricated electrodes namely, $TiO_2/BiSbS_3$, TiO_2/CdS, and $TiO_2/CdS/BiSbS_3$ under chopped solar irradiation. Different number cycles of CdS on TiO_2 and different loading times for $BiSbS_3$ electrode photoactivity is given in the supporting information (Figure S8). Fabricated electrodes were used as working electrode whereas Ag/AgCl and Pt were used as reference electrode and counter electrode, respectively. LSV (linear sweep voltammetry) for bare $BiSbS_3$ is given in Figure S8. The photocatalytic performance of the electrodes were examined under a neutral aqueous electrolyte (0.1 M Na_2SO_4) with a pH of 6.8. The photocurrent response was recorded using current-voltage curves. Under chopped solar light illumination, the fabricated photoanodes

$TiO_2/BiSbS_3$, TiO_2/CdS, and $TiO_2/CdS/BiSbS_3$ exhibited good current density values of 2.1, 3.6, and 5 $mA{\cdot}cm^{-2}$, respectively at 1.23 V vs. RHE. The efficiency for $TiO_2/BiSbS_3$, TiO_2/CdS, and $TiO_2/CdS/BiSbS_3$ composites is stated in terms of STH conversion, which is determined at 1.8, 2.2, and 3.8% at 0.3, 0.29, and 0.52 V vs. RHE, respectively (Figure 5a,b). The improved PEC activity of the ternary photoanode was renowned to the sensitization of $BiSbS_3$ to create e^-/h^+ pairs and a facile charge transfer of electrons from CB of $BiSbS_3$ to CB of CdS to CB of TiO_2, when hydrogen evolution takes place at counter electrode, whereas hole transfer goes in opposite direction from VB of TiO_2 to VB of CdS to VB of $BiSbS_3$ and oxygen evolution reaction takes place on the electrode surface. This whole process improves the charge separation and suppresses the charge recombination, thus resulting in an enhancement of photocatalytic activity. $BiSbS_3$ and CdS play the role of sensitizer and co-sensitizer to improve the absorption capacity of solar spectrums for fabricated electrodes and boost the PEC performance of the electrodes.

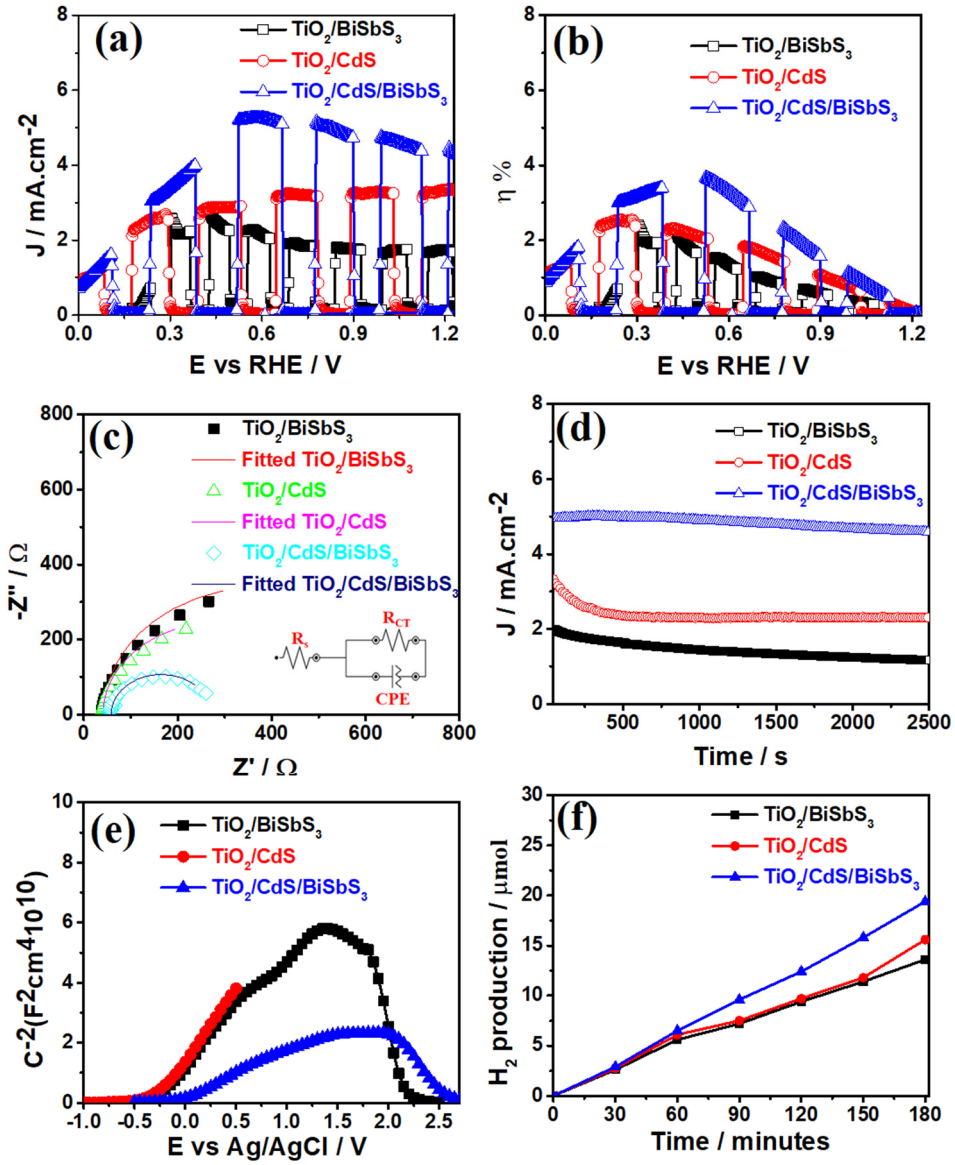

Figure 5. Photocatalytic properties of fabricates electrodes $TiO_2/BiSbS_3$, TiO_2/CdS, and $TiO_2/CdS/BiSbS_3$ (**a**) LSV curves, (**b**) Solar to hydrogen efficiency plot, (**c**) EIS studies, (**d**) Photostability response, (**e**) Mott–Schottky (M-S) plot and, (**f**) Temporal evolution of H_2 gas (0.1 M Na_2SO_4).

To examine the long-term stability of fabricated electrodes $TiO_2/BiSbS_3$, TiO_2/CdS, and $TiO_2/CdS/BiSbS_3$, chronoamperometry measurements were done. As displayed in

Figure 5d, ternary heterojunction exhibited excellent stability for over 2500 s under continuous solar light illumination at 1.23 V vs. RHE under a neutral aqueous electrolyte, and the photocurrent values are in support with those obtained from LSV for TiO_2/CdS/$BiSbS_3$, whereas, TiO_2/$BiSbS_3$ and TiO_2/CdS displayed instability due to photocorrosion and sulfur dissolution in water. The n-type CdS is well known for its photocorrosive nature. Due to the addition of narrow bandgap p-type material $BiSbS_3$ as a co-sensitizer in the PEC process, the photostability can be enhanced and the photocorrosion of CdS is decreased. After 2000 s, composite electrodes could undergo photocorrosion, which is why it shows a sudden change in stability, whereas in the case TiO_2/CdS, a continuous decrement in the current could be observed due to corrosion, and the TiO_2/$BiSbS_3$ electrode was stable after initial decrement. CdS and $BiSbS_3$ show synergetic effects and suppress the charge recombination. Proper band edge positions help timely consumption of photoinduced charge carriers and improves the photostability under neutral electrolyte. These results indicate that ternary heterostructures for hydrogen production have excellent photostability and PEC efficiency.

The charge transfer kinetics at the photoelectrode/electrolyte interface was investigated using EIS (Electrochemical Impedance Spectroscopy) measurements. The EIS experiment was performed in an alkaline aqueous solution at an open-circuit potential under solar light irradiation to understand the interfacial charge transfer resistance. TiO_2/$BiSbS_3$, TiO_2/CdS, and TiO_2/CdS/$BiSbS_3$ photoanodes are estimated to be have R_{ct} values of 952, 504, and 222 ohm, respectively. The composite has a smaller R_{ct} than other photoanodes, and a low Rct for TiO_2/CdS/$BiSbS_3$ signifies efficient charge separation and transportation. The p-type $BiSbS_3$ and n-type CdS extend the capacity of absorbing extra solar light and enhances the facile charge transportation and transfer. Furthermore, according to the Bode phase plots of TiO_2/$BiSbS_3$, TiO_2/CdS, and TiO_2/CdS/$BiSbS_3$ photoanodes, proper band edge positions of TiO_2, CdS, and $BiSbS_3$ can significantly promote a fast charge transfer. This is in good agreement with phase angle shifting and decrement in charge transfers at different frequencies as shown in Figure S10 [43].

Furthermore, the semiconducting properties of the electrodes were also analyzed using Mott–Schottky (MS) plots in Figure 5e, which reveal that TiO_2/CdS has an n-type behavior of the electrodes with positive slop, whereas TiO_2/$BiSbS_3$ and TiO_2/CdS/$BiSbS_3$ have inverted V-shape plots that confirm the p-n junction formation between n-type TiO_2, TiO_2/CdS, and p-type $BiSbS_3$ [44]. Typically, a high charge carrier density is delivered by the electrode with the minimum slope for the M-S plot. Impressively, compared to the TiO_2/CdS or TiO_2/$BiSbS_3$ electrodes, the TiO_2/CdS/$BiSbS_3$ photoelectrode displays a lower slope with a high charge carrier concentration in Figure 5e. Additionally, all of the electrodes' flat band potentials (V_{FB}) range from 0.1 to −0.5 V. This evidence supports the photogenerated carriers' quick transport or poor recombination as well as the elevated PEC hydrogen generation. As shown in Figure S9, TiO_2, CdS, and $BiSbS_3$ M-S plots demonstrate that TiO_2 and CdS are n-type semiconductors, whereas $BiSbS_3$ is a p-type semiconductor. In theory, the flatband band (V_{FB}) is assumed to be position of the conduction band for n-type materials and the valance band for p-type materials [45]. TiO_2 has a CB value of −0.41 eV vs. Ag/AgCl, CdS has a CB value of −0.61 eV vs. Ag/AgCl, and $BiSbS_3$ has a VB value of +0.6 eV vs. Ag/AgCl after extrapolation of the M-S plots of independent materials. The VB of TiO_2 and CdS, on the other hand, are 2.82 and 2.01 eV vs. Ag/AgCl, respectively, and are nearly equal to the calculated values from cyclic voltammetry calculations. $BiSbS_3$ has a CB of −1.2 eV versus Ag/AgCl.

Under solar light irradiation, gas chromatography (GC) was used to measure the evolution of H_2 at various time intervals. The usual H_2 production as a function of time from TiO_2/$BiSbS_3$, TiO_2/CdS and TiO_2/CdS/$BiSbS_3$ photoanodes were examined in a three-electrode system at 1.23 V vs. RHE in a neutral medium (Na_2SO_4) as shown in Figure 5f. Due to improved band alignment and reduced charge recombination, the TiO_2/CdS/$BiSbS_3$ photoanode provides superior H_2 evolution of 19.8 µmol over 3 h TiO_2/$BiSbS_3$ (12.6 µmol)

and TiO_2/CdS (15.2 µmol) electrodes. As a result, of all the fabricated electrodes, PEC performance and H_2 evolution performances are in good agreement.

3. Reaction Mechanism

Figure 6 depicts the reaction mechanism in which TiO_2/CdS/$BiSbS_3$ exhibits improved PEC performance. According to cyclic voltammetry (CV) and optical studies, the conduction band (CB) and valence band (VB) of $BiSbS_3$ are −3.49 eV and −5.34 eV vs. vacuum level, respectively, whereas TiO_2 CB and VB are −4.09 eV and −7.32 eV, respectively. SILAR successfully fabricated CdS has band-edge positions between TiO_2 and $BiSbS_3$, with determined CB and VB values of −3.94 and −6.52 eV, respectively, vs. vacuum level. In addition, optical measurements and CV analysis are used to derive the CB and VB positions to understand the charge transfer phenomena. CB values were calculated using CV plots as shown in Figure S11a–c. As a result, CB was calculated from the reduction or oxidation potential from CV, such as for bare TiO_2, CdS, and $BiSbS_3$ and the bandgap was calculated from UV-visible spectroscopy. When n-type TiO_2/CdS and p-type $BiSbS_3$ came in contact to establish a p–n junction, band bending would have taken place at the interface to acquire a similar Fermi level, producing an upward transition in TiO_2/CdS and a downward transition in $BiSbS_3$. Therefore, when anodic TiO_2/CdS was combined with cathodic $BiSbS_3$, the band edge sites of the different components changed dramatically as a result of band bending and Fermi level matching, resulting in a change in charge transfer path. Afterwards, TiO_2/CdS/$BiSbS_3$ p-n heterojunction emerged, and electrons at the junction migrated toward the cathodic $BiSbS_3$ region, having left h^+ ions in the n-type TiO_2/CdS region [46]. Likewise, the h^+ ions at the TiO_2/CdS/$BiSbS_3$ p-n heterojunction interface inclined to transfer into the anodic TiO_2/CdS, establishing a space charge barrier at the TiO_2/CdS/$BiSbS_3$ junction. This induced an electric field, which led photoinduced electrons and holes to travel backwards. Photoinduced charge carriers in TiO_2/CdS/$BiSbS_3$ were vastly separated as a result, allowing for better charge separation [47]. As a result, the band bending could significantly impact depending on the applied bias potential. During the electrochemical reaction, the depletion layer's capacitance (at the interface) will be at its lowest, having allowed charge transfer to move more smoothly. During cathodic polarization, the capacitance at the interface rises, limiting charge transport. Overall, the evaluation demonstrates that the construction of a p-n junction, which easily dispersed photoinduced charges, is effective in the PEC aspects of the TiO_2/CdS/$BiSbS_3$ photoelectrode. The enhanced PEC performance was attributed to the improved driving force for the interface reactions promoted by $BiSbS_3$ as well as the low charge transfer resistances throughout electrode/electrolyte interface [48]. Possible electrons transport from $BiSbS_3$ (CB) to CdS (CB) to TiO_2 (CB), which are responsible for HER at CE, whereas holes move in the opposite direction and give ORE at the electrode/electrolyte surface as shown in Figure 6.

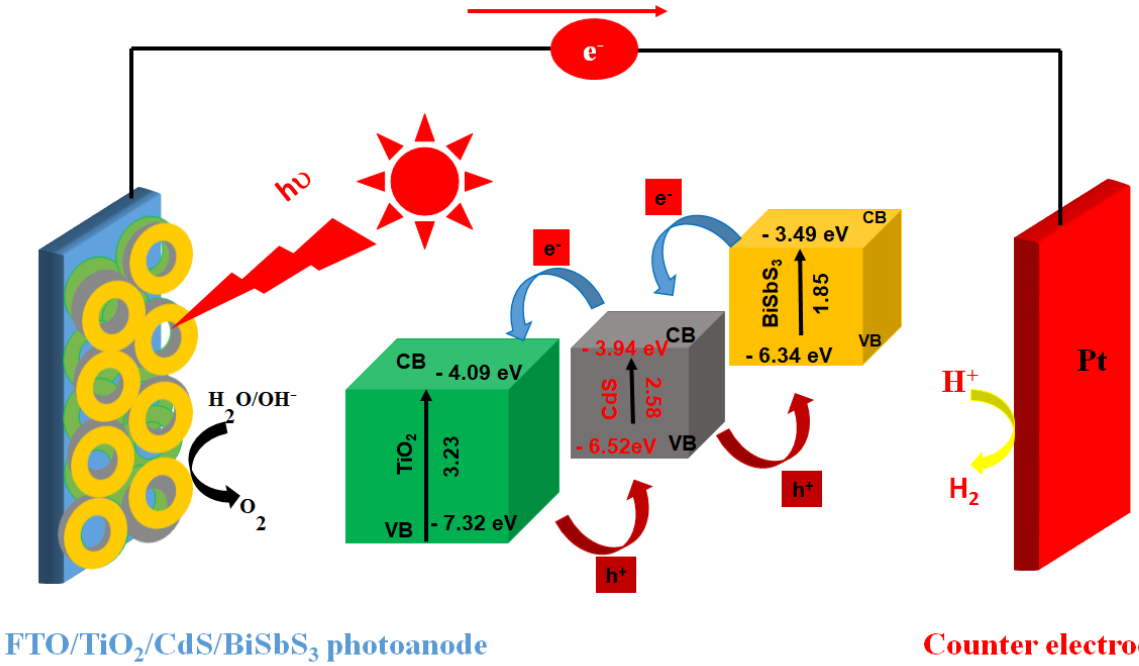

Figure 6. Possible reaction mechanism for efficient charge transfer in TiO_2/CdS/$BiSbS_3$ photoanode.

4. Materials and Methods

4.1. Chemicals

Cadmium acetate dihydrate ($Cd(CH_3COO)_2 \cdot 2H_2O$ (>98%,) Bismuth chloride (>98%), thioacetamide (>99%), sodium sulfide (>99%), antimony chloride(>98%), and sodium sulfate (>99%), Dimethyl sulfoxide (99.9%) (DMSO) were purchased from sigma Aldrich (St. Louis, MO, USA). Dyesol TiO_2 paste was used. Fluorine-doped tin oxide (FTO) conductive glass with the resistance 22 Ω/cm^2 was obtained from Sigma Aldrich (St. Louis, MO, USA) and FTO substrate was pre-cleaned with methanol and acetone.

4.2. Characterization

The absorption spectra of the synthesized electrodes were recorded on a UV-Vis spectrophotometer (Shimadzu UV-3600 Wolflabs, Colenso House, 1 Deans Lane, Pocklington, York). A Horiba Flouromax-4 fluorescence spectrometer (2 Miyanohigashi, Kisshoin, Minami-ku, Kyoto 601-8510, Japan) was used to measure the fluorescence spectra of electrodes. Powder X-ray diffraction (XRD, Malvern Panalytical Ltd., Worcestershire, UK) patterns of samples were measured on a PANalytical, Xpert PRO instrument. Surface morphologies of the samples were analyzed using a field emission scanning electron microscope (FESEM-Zeiss supra 40, Peabody, MA 01960, USA). The chemical stoichiometry of the TiO_2/CdS/$BiSbS_3$ fabricated electrode was characterized using an X-ray photoelectron spectroscopy (XPS; AXIS Supra-Kratos analytical spectrophotometer, (Shimadzu Corp., Kyoto, Japan) with Mg Kα monochromatic excited radiation of 1253.6 eV. High-resolution transmission electron microscope (HR-TEM, Berlin, Germany) images were recorded using a TECNAI G-2 FEI instrument operating at 300 kV with samples deposited on copper grids. PEC measurements were performed in an aqueous electrolyte of 0.1 M Na_2SO_4 using a three-electrode system with fabricated films used as a working electrode, and Pt and Ag/AgCl as the counter and reference electrodes, respectively (Herisau, Switzerland). Current versus potential (I-V) characteristics of photoanodes were recorded using a LOT-Oriel-Autolab (Herisau Switzerland) with a 150 W Xenon arc lamp with 100 mW cm^{-2} intensity (1.5 Airmass filter). Chronoamperometric (I-t) studies, cyclic voltammetry, and electrochemical impedance spectra

(EIS) were measured on an Autolab PGSTAT 302N equipped with NOVA 2.1 software. A Trace1310 GC equipped with a TCD was used to quantify hydrogen gas. ZsimWin software was used to fit impedance data in a Cole-Cole circuit (Thames, UK).

4.3. TiO_2 Synthesis

The photoanode fabrication was as follows: the TiO_2 paste was coated onto a pre-cleaned FTO plate using the doctor blading method, which was followed by annealing the plate at 500 °C for 30 min. A layer of TiO_2 was formed on FTO. Further, TiO_2 films were immersed in a 40 mM $TiCl_4$ solution maintained at 70 °C for 30 min. The resulting films were rinsed with deionized water and annealed at 500 °C for 30 min to provide a uniform TiO_2 electrode [49].

4.4. CdS Coating over TiO_2 Photoanode

TiO_2 was vertically dipped in a cadmium precursor (0.1 M $(Cd(CH_3COO)_2 \cdot 2H_2O$ in CH_3OH) for 2 min, rinsed with methanol, and dried at 65 °C. This film was successively immersed in a sulfur precursor solution (0.1 M $Na_2S \cdot 9H_2O$ in CH_3OH)) for 2 min, which was followed by rinsing with methanol and drying in a hot air oven at 65 °C. This was one SILAR cycle of CdS growth on the TiO_2 film. Five SILAR cycles were performed to obtain the desirable TiO_2/CdS composite [37]

4.5. $BiSbS_3$ Synthesis

$BiSbS_3$ films were deposited on FTO by the CBD method. To deposit $BiSbS_3$ thin film onto FTO, a solution of bismuth chloride (0.1 M) and antimony chloride (0.1 M) were mixed in a beaker and sonicated for 5 min. Then, thioacetaamide (0.1 M) was mixed into the above mixture. The obtained mixture was stirred for 4 h, which then turned into a transparent solution. The FTO of the fixed area was kept inside the beaker containing transparent solution for 8 h. Thin films of different thicknesses were obtained after the deposition time period. The films were taken out of the bath, dried, and preserved. The color of the film was orange. Then, obtained films were kept in n argon atmosphere for 30 min at 300 °C. Then, $BiSbS_3$ colors changed to a brownish color [22].

4.6. Fabrication of FTO/TiO_2/CdS/$BiSbS_3$ Photoelectrode

Bare TiO_2, TiO_2/$BiSbS_3$, and TiO_2/CdS photoelectrode fabrication have been given in the supporting information. $BiSbS_3$ was coated over FTO/TiO_2/CdS by simple a CBD method for 24 h. In total, 0.1 M bismuth chloride, 0.1 M antimony chloride, and 0.1 M thioacetamide were used as bismuth, antimony, and sulfur precursors, respectively. Firstly, Bi^{+3}, Sb^{+3}, and S^{-2} were mixed in one beaker and kept under stirring for 24 h until a transparent solution was obtained. Then, the TiO_2/CdS photoelectrode was dipped in this solution for 12 h and an orange color film was formed. To obtain the final product, orange colored film was annealed at 300 °C for 1 h under an argon atmosphere to obtain a crystalline film. The FTO/TiO_2/CdS/$BiSbS_3$ photoanode color changed to a brownish color from orange after annealing. A schematic representation of the ternary heterojunction photoelectrode has been given in Scheme 1.

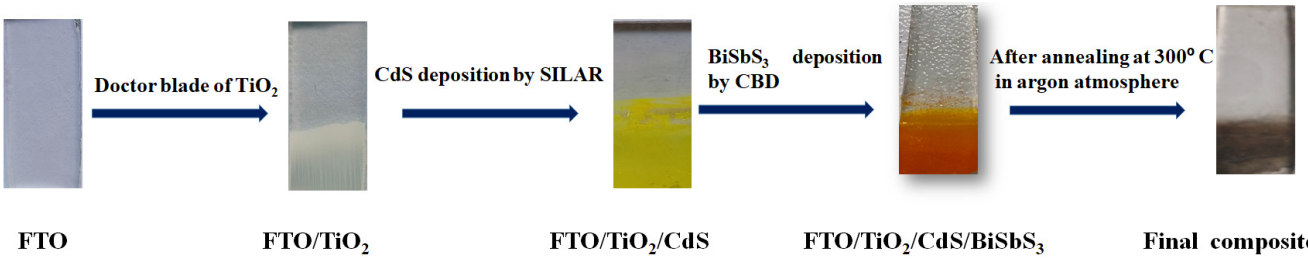

Scheme 1. Schematic representation of ternary TiO_2/CdS/$BiSbS_3$ heterojunction photoelectrode.

5. Conclusions

In this study, we have fabricated ternary heterojunction $TiO_2/CdS/BiSbS_3$ as an efficient photoelectrode over a conductive substrate FTO using the doctor blade method followed by SILAR and CBD methods. Ternary heterojunction exhibited higher photocurrent density of 5 $mA{\cdot}cm^{-2}$ at 1.23V RHE and 3.8% STH efficiency at 0.52 V vs. RHE, whereas binary photoelectrodes, $TiO_2/BiSbS_3$ and TiO_2/CdS, displayed 2.1 and 3.6 $mA{\cdot}cm^{-2}$ photocurrent densities and 1.8 and 2.2% STH efficiencies, respectively. Ternary electrode showed good photostability over 2500 s and better PEC performance compared to both the binary electrodes. PL and EIS studies have explained less charge recombination over binary electrodes. FESEM demonstrated that TiO_2 has nanoparticles morphology and CdS has dendrite morphology, whereas $BiSbS_3$ gives nanosphere morphology. HRTEM, XPS, and XPS proved that fabrication of electrodes have been done without any impurity. $TiO_2/CdS/BiSbS_3$ photoanode produces more hydrogen than $TiO_2/BiSbS_3$ and TiO_2/CdS. CdS and $BiSbS_3$ exhibit synergetic effects that enhance solar harvesting efficiency and suppress the charge carrier recombination. The p–n junction constructed by $TiO_2/CdS/BiSbS_3$ enabled improved charge separation and propagation, including the mitigation of the electron–hole recombination, resulting in an improved PEC hydrogen production efficiency. The presented results demonstrate that deploying a $BiSbS_3$ film to construct a p–n junction at the TiO_2/CdS heterojunction can significantly enhance PEC water splitting performance.

Supplementary Materials: The following supporting information can be downloaded at: https://www.mdpi.com/article/10.3390/catal12101117/s1, Figure S1: Fabricated electrodes UV-visible spectra of (a) TiO_2 and (b) CdS; Figure S2: Tauc's plot of (a) TiO_2 and CdS and (b) $BiSbS_3$; Figure S3: PL spectra of fabricated electrodes; Figure S4: XRD pattern of CdS; Figure S5: XPS of (a) C 1s and (b) Survey scan of fabricated electrode $TiO_2/CdS/BiSbS_3$; Figure S6: Elemental mapping for (a) Ti, (b) O, (c) S, (d) Bi, (e) Cd, and (f) Sb; Figure S7: (a) HRTEM image of TiO_2/CdS composite and (b) lattice fringes; Figure S8: LSV of $BiSbS_3$ in 0.1M Na_2SO_4; Figure S9: Mott–Schottky plots (a) TiO_2 and CdS and (b) $BiSbS_3$; Figure S10: Bode phase plot for fabricated electrodes $TiO_2/BiSbS3$, TiO_2/CdS, and $TiO_2/CdS/BiSbS_3$; Figure S11: CV plots for (a) TiO_2, (b) CdS, and (c) $BiSbS_3$; Figure S12: SEM and EDS image of TiO_2 nanoparticles; Figure S13: LSV plots for (a) $TiO_2/BiSbS_3$ and (b) TiO_2/CdS; Table S1: Impedance data after fitting plots of the $TiO_2/BiSbS_3$, TiO_2/CdS, and $TiO_2/CdS/BiSbS_3$.

Author Contributions: Contribution statement for the authors of CRediT. The first author is B.M. He planned the scheme, worked on it, and then wrote the manuscript. M.K. and A.K. contributed to the characterization of the fabricated samples. The manuscript's typos and English grammar were checked by G.N.S., R.N. and P.S. D.S. helped in characterization. The works corresponding author, C.S., assisted in its creation and wrote the manuscript. All authors have read and agreed to the published version of the manuscript.

Funding: This research received no external funding.

Data Availability Statement: The data presented in this study are available on request from the corresponding author.

Acknowledgments: BM and MK are grateful for the CSIR research fellowship from India. CS would like to acknowledge the support from the JICA Friendship 2.0 grant.

Conflicts of Interest: There is no conflict of interest.

References

1. Miller, E.L. Photoelectrochemical water splitting. *Energy Environ. Sci.* **2015**, *8*, 2809–2810. [CrossRef]
2. Graätzel, M. Photoelectrochemical cells. *Nature* **2001**, *414*, 338–344. [CrossRef] [PubMed]
3. Sivula, K.; van de Krol, R. Semiconducting materials for photoelectrochemical energy conversion. *Nat. Rev. Mater.* **2016**, *1*, 15010. [CrossRef]
4. Sun, B.; Zhou, W.; Li, H.; Ren, L.; Qiao, P.; Li, W.; Fu, H. Synthesis of Particulate Hierarchical Tandem Heterojunctions toward Optimized Photocatalytic Hydrogen Production. *Adv. Mater.* **2018**, *30*, 1804282. [CrossRef]
5. Tee, S.Y.; Win, K.Y.; Teo, W.S.; Koh, L.D.; Liu, S.; Teng, C.P.; Han, M.Y. Recent progress in energy-driven water splitting. *Adv. Sci.* **2017**, *4*, 1600337. [CrossRef]

6. Warren, S.C.; Voïtchovsky, K.; Dotan, H.; Leroy, C.M.; Cornuz, M.; Stellacci, F.; Hébert, C.; Rothschild, A.; Grätzel, M. Identifying champion nanostructures for solar water-splitting. *Nat. Mater.* **2013**, *12*, 842. [CrossRef]
7. Ni, M.; Leung, M.K.; Leung, D.Y.; Sumathy, K. A review and recent developments in photocatalytic water-splitting using TiO_2 for hydrogen production. *Renew. Sustain. Energy Rev.* **2007**, *11*, 401–425. [CrossRef]
8. Subramanyam, P.; Meena, B.; Suryakala, D.; Subrahmanyam, C. TiO_2 photoanodes sensitized with Bi_2Se_3 nanoflowers for visible–near-infrared photoelectrochemical water splitting. *ACS Appl. Nano Mater.* **2021**, *4*, 739–745. [CrossRef]
9. Subramanyam, P.; Meena, B.; Sinha, G.N.; Deepa, M.; Subrahmanyam, C. Decoration of plasmonic Cu nanoparticles on WO_3/Bi_2S_3 QDs heterojunction for enhanced photoelectrochemical water splitting. *Int. J. Hydrogen Energy* **2020**, *45*, 7706–7715. [CrossRef]
10. Subramanyam, P.; Meena, B.; Suryakala, D.; Subrahmanyam, C. Influence of Bi–Cu microstructure on the photoelectrochemical performance of $BiVO_4$ photoanode for efficient water splitting. *Sol. Energy Mater. Sol. Cells* **2021**, *232*, 111354. [CrossRef]
11. Shao, M.; Ning, F.; Wei, M.; Evans, D.G.; Duan, X. Hierarchical nanowire arrays based on ZnO core layered double hydroxide shell for largely enhanced photoelectrochemical water splitting. *Adv. Funct. Mater.* **2014**, *24*, 580–586. [CrossRef]
12. Radecka, M.; Wnuk, A.; Trenczek-Zajac, A.; Schneider, K.; Zakrzewska, K. TiO_2/SnO_2 nanotubes for hydrogen generation by photoelectrochemical water splitting. *Int. J. Hydrogen Energy* **2015**, *40*, 841–851. [CrossRef]
13. Sharma, D.; Satsangi, V.R.; Shrivastav, R.; Waghmare, U.V.; Dass, S. Understanding the photoelectrochemical properties of nanostructured CeO_2/Cu_2O heterojunction photoanode for efficient photoelectrochemical water splitting. *Int. J. Hydrogen Energy* **2016**, *41*, 18339–18350. [CrossRef]
14. Choi, M.J.; Kim, T.L.; Choi, K.S.; Sohn, W.; Lee, T.H.; Lee, S.A.; Park, H.; Jeong, S.Y.; Yang, J.W.; Lee, S.; et al. Controlled Band Offsets in Ultrathin Hematite for Enhancing the Photoelectrochemical Water Splitting Performance of Heterostructured Photoanodes. *ACS Appl. Mater. Interfaces* **2022**, *14*, 7788–7795. [CrossRef] [PubMed]
15. Fujishima, A.; Honda, K. Electrochemical photolysis of water at a semiconductor electrode. *Nature* **1972**, *238*, 37. [CrossRef]
16. Yoo, I.H.; Kalanur, S.S.; Seo, H. A nanoscale p–n junction photoelectrode consisting of an NiO_x layer on a TiO_2/CdS nanorod core-shell structure for highly efficient solar water splitting. *Appl. Catal. B Environ.* **2019**, *250*, 200–212. [CrossRef]
17. Subramanyam, P.; Vinodkumar, T.; Deepa, M.; Subrahmanyam, C. Gold nanoparticle decorated bismuth sulfide nanorods for enhanced photoelectrochemical hydrogen production. *J. Mater. Chem. C* **2019**, *7*, 6398–6405. [CrossRef]
18. Ibadurrohman, M.; Hellgardt, K. Morphological modification of TiO_2 thin films as highly efficient photoanodes for photoelectrochemical water splitting. *ACS Appl. Mater. Interfaces* **2015**, *7*, 9088–9097. [CrossRef]
19. Wang, C.; Chen, Z.; Jin, H.; Cao, C.; Li, J.; Mi, Z. Enhancing visible-light photoelectrochemical water splitting through transition-metal doped TiO_2 nanorod arrays. *J. Mater. Chem. A* **2014**, *2*, 17820–17827. [CrossRef]
20. Yin, X.L.; Liu, J.; Jiang, W.J.; Zhang, X.; Wan, J.S.H.L.J. Urchin-like Au@CdS/WO_3 micro/nano heterostructure as a visible-light driven photocatalyst for efficient hydrogen generation. *Chem. Commun.* **2015**, *51*, 13842–13845. [CrossRef]
21. Quang, N.D.; Hien, T.T.; Chinh, N.D.; Kim, D.; Kim, C.; Kim, D. Transport of photo-generated electrons and holes in TiO_2/CdS/CdSe core-shell nanorod structure toward high performance photoelectrochemical cell electrode. *Electrochim. Acta* **2019**, *295*, 710–718. [CrossRef]
22. Meena, B.; Kumar, M.; Gupta, S.; Sinha, L.; Subramanyam, P.; Subrahmanyam, C. Rational design of $TiO_2/BiSbS_3$ heterojunction for efficient solar water splitting. *Sustain. Energy Technol. Assess* **2022**, *49*, 101775. [CrossRef]
23. Walter, M.G.; Warren, E.L.; McKone, J.R.; Boettcher, S.W.; Mi, Q.; Santori, E.A.; Lewis, N.S. Solar water splitting cells. *Chem. Rev.* **2010**, *110*, 6446–6473. [CrossRef] [PubMed]
24. Liu, Z.; Yan, L. High-efficiency p–n junction oxide photoelectrodes for photoelectrochemical water splitting. *Phys. Chem. Chem. Phys.* **2016**, *18*, 31230–31237. [CrossRef]
25. Chen, Y.C.; Yeh, H.Y.; Popescu, R.; Gerthsen, D.; Hsu, Y.K. Solution–processed $Cu_2O/ZnO/TiO_2$/Pt nanowire photocathode for efficient photoelectrochemical water. *J. Alloys Compd.* **2022**, *899*, 163348. [CrossRef]
26. Xu, J.Z.Q.; Feng, Z.; Li, M.; Li, C. Importance of the relationship between surface phases and photocatalytic activity of TiO_2. *Angew. Chem.* **2008**, *120*, 1790–1793.
27. Pan, Q.; Zhang, C.; Xiong, Y.; Mi, Q.; Li, D.; Zou, L.; Huang, Q.; Zou, Z.; Yang, H. Boosting charge separation and transfer by plasmon-enhanced $MoS_2/BiVO_4$ p–n heterojunction composite for efficient photoelectrochemical water splitting. *ACS Sustain. Chem. Eng.* **2018**, *6*, 6378–6387. [CrossRef]
28. Lv, P.; Fu, W.; Yang, H.; Sun, H.; Chen, Y.; Ma, J.; Zhou, X.; Tian, L.; Zhang, W.; Li, M.; et al. Simple synthesis method of Bi_2S_3/CdS quantum dots cosensitized TiO_2 nanotubes array with enhanced photoelectrochemical and photocatalytic activity. *CrystEngComm* **2013**, *15*, 7548–7555. [CrossRef]
29. Ai, G.; Li, H.; Liu, S.; Mo, R.; Zhong, J. Solar water splitting by TiO_2/CdS/Co–Pi nanowire array photoanode enhanced with Co–Pi as hole transfer relay and CdS as light absorber. *Adv. Funct. Mater.* **2015**, *25*, 5706–5713. [CrossRef]
30. Ansari, M.Z.; Singh, S.; Khare, N. Visible light active CZTS sensitized CdS/TiO_2 tandem photoanode for highly efficient photoelectrochemical hydrogen generation. *Sol. Energy* **2019**, *181*, 37–42. [CrossRef]
31. Yang, C.; Chen, Y.; Chen, T.; Rajendran, S.; Zeng, Z.; Qin, J.; Zhang, X. A long-standing polarized electric field in TiO_2@ $BaTiO_3$/CdS nanocomposite for effective photocatalytic hydrogen evolution. *Fuel* **2022**, *314*, 122758. [CrossRef]
32. Li, D.; Yang, C.; Rajendran, S.; Qin, J.; Zhang, X. Nanoflower-like Ti_3CN@ TiO_2/CdS heterojunction photocatalyst for efficient photocatalytic water splitting. *Int. J. Hydrogen Energy* **2021**, *47*, 9580–19589. [CrossRef]

33. Dang, W.; Xu, K.; Zhang, L.; Qian, Y. Fabrication of multilayer 1D TiO_2/CdS/ZnS with high photoelectrochemical performance and enhanced stability. *J. Alloys Compd.* **2021**, *886*, 161329. [CrossRef]
34. Kang, X.; Chaperman, L.; Galeckas, A.; Ammar, S.; Mammeri, F.; Norby, T.; Chatzitakis, A. Water Vapor Photoelectrolysis in a Solid-State Photoelectrochemical Cell with TiO_2 Nanotubes Loaded with CdS and CdSe Nanoparticles. *ACS Appl. Mater. Interfaces* **2021**, *13*, 46875–46885. [CrossRef] [PubMed]
35. Elbakkay, M.H.; el Rouby, W.M.; Mariño-López, A.; Sousa-Castillo, A.; Salgueirino, V.; El-Dek, S.I.; Farghali, A.A.; Correa-Duarte, M.A.; Millet, P. One-pot synthesis of TiO_2/Sb_2S_3/RGO complex multicomponent heterostructures for highly enhanced photoelectrochemical water splitting. *Int. J. Hydrogen Energy* **2021**, *46*, 31216–31227. [CrossRef]
36. Zuo, Y.; Chen, J.; Yang, H.; Zhang, M.; Wang, Y.; He, G.; Sun, Z. Facile synthesis of TiO_2/In_2S_3/CdS ternary porous heterostructure arrays with enhanced photoelectrochemical and visible-light photocatalytic properties. *J. Mater. Chem. C* **2019**, *7*, 9065–9074. [CrossRef]
37. Meena, B.; Subramanyam, P.; Suryakala, D.; Biju, V.; Subrahmanyam, C. Efficient solar water splitting using a CdS quantum dot decorated TiO_2/Ag_2Se photoanode. *Int. J. Hydrogen Energy* **2021**, *46*, 34079–34088. [CrossRef]
38. Patra, B.K.; Khilari, S.; Bera, A.; Mehetor, S.K.; Pradhan, D.; Pradhan, N. Chemically filled and Au-coupled $BiSbS_3$ nanorod heterostructures for photoelectrocatalysis. *Chem. Mater.* **2017**, *29*, 1116–1126. [CrossRef]
39. Jiang, F.; Yan, T.; Chen, H.; Sun, A.; Xu, C.; Wang, X. A g-C_3N_4–CdS composite catalyst with high visible-light-driven catalytic activity and photostability for methylene blue degradation. *Appl. Surf. Sci.* **2014**, *295*, 164–172. [CrossRef]
40. Kumar, K.A.; Chandana, L.; Ghosal, P.; Subrahmanyam, C. Simultaneous photocatalytic degradation of p-cresol and Cr (VI) by metal oxides supported reduced graphene oxide. *Mol. Catal.* **2018**, *451*, 87–95. [CrossRef]
41. Martha, S.; Mansingh, S.; Parida, K.M.; Thirumurugan, A. Exfoliated metal free homojunction photocatalyst prepared by a biomediated route for enhanced hydrogen evolution and Rhodamine B degradation. *Mater. Chem. Front.* **2017**, *1*, 1641–1653. [CrossRef]
42. Jiang, D.; Chen, L.; Zhu, J.; Chen, M.; Shi, W.; Xie, J. Novel p–n heterojunction photocatalyst constructed by porous graphite-like C_3N_4 and nanostructured BiOI: Facile synthesis and enhanced photocatalytic activity. *Dalton Trans.* **2013**, *42*, 15726–15734. [CrossRef] [PubMed]
43. Rammelt, U.; Hebestreit, N.; Fikus, A.; Plieth, W. Investigation of polybithiophene/n-TiO_2 bilayers by electrochemical impedance spectroscopy and photoelectrochemistry. *Electrochim. Acta* **2001**, *46*, 2363–2371. [CrossRef]
44. Ye, S.; Shi, W.; Liu, Y.; Li, D.; Hang, Y.; Chi, H. Unassisted Photoelectrochemical Cell with Multimediator Modulation for Solar Water Splitting Exceeding 4% Solar-to-Hydrogen Efficiency. *J. Am. Chem. Soc.* **2021**, *143*, 12499–12508. [CrossRef]
45. Zhang, X.; Zhang, B.; Cao, K.; Brillet, J.; Chen, J.; Wang, C.; Shen, Y. A perovskite solar cell-TiO_2@ $BiVO_4$ photoelectrochemical system for direct solar water splitting. *J. Mater. Chem A* **2015**, *3*, 21630–21636. [CrossRef]
46. Yang, H.B.; Miao, J.; Hung, S.F.; Huo, F.; Chen, H.M.; Liu, B. table quantum dot photoelectrolysis cell for unassisted visible light solar water splitting. *ACS Nano* **2014**, *8*, 10403–10413. [CrossRef]
47. Kumar, M.; Ghosh, C.C.; Ma, B.M.T.; Subrahmanyam, C. Plasmonic Au nanoparticle sandwiched $CuBi_2O_4$/Sb2S3 photocathode with multi-mediated electron transfer for efficient solar water splitting. *Sustain. Energy Fuels* **2022**, *6*, 3961–3974. [CrossRef]
48. Zhu, Y.; Liu, Y.; Ai, Q.; Gao, G.; Yuan, L.; Fang, Q.; Tian, X.; Zhang, X.; Egap, E.; Ajayan, P.M.; et al. In situ synthesis of lead-free halide perovskite–COF nanocomposites as photocatalysts for photoinduced polymerization in both organic and aqueous phases. *ACS Mater. Lett.* **2022**, *4*, 464–471. [CrossRef]
49. Subramanyam, P.; Kumar, P.N.; Deepa, M.; Subrahmanyam, C.; Ghosal, P. Bismuth sulfide nanocrystals and gold nanorods increase the photovoltaic response of a TiO_2/CdS based cell. *Sol. Energy Mater Sol. Cells* **2017**, *159*, 296–306. [CrossRef]